Fast Calculation of Icing Cloud Parameters Based on POD_Kriging Surrogate Model

LI Tingyu[1,2], *REN Jinghao*[1,2], *WANG Qiang*[1,2], *YI Xian*[1,2*]

1. Low Speed Aerodynamic Institute, China Aerodynamics Research and Development Center, Mianyang 621000, P. R. China;

2. Anti/De-icing Key Laboratory, China Aerodynamics Research and Development Center, Mianyang 621000, P. R.China

(Received 10 March 2023; revised 15 June 2023; accepted 10 August 2023)

Abstract: The distribution of ice cloud parameters is of great significance to the analysis of aircraft icing. In order to obtain these parameters, traditional high-fidelity numerical simulation techniques have low computational efficiency and are difficult to apply in engineering scenarios that require real-time evaluation of icing. To overcome this difficulty, a non-intrusive surrogate model is proposed by proper orthogonal decomposion (POD) model coupled with the Kriging technology. The model takes four flight parameters and two cloud parameters as input variables. The model outputs are liquid water content (LWC) and droplet collection efficiency. A quasi-three-dimensional NACA0012 airfoil is adopted to verify the accuracy and computational efficiency of the model. The numerical results of the four test cases show that the POD_Kriging model is able to produce satisfactory results for the statistical quantities of interest. It is found that the developed surrogate model is computationally more efficient than the classical FENSAP-ICE for simulation of icing cloud field.

Key words: icing cloud parameters; surrogate model; proper orthogonal decomposion (POD); Kriging; fast calculation

CLC number: V181;V321.229 **Document code:** A **Article ID:** 1005-1120(2023)S1-0001-12

0 Introduction

Numerous flight practices have shown that when an aircraft passes through a cloud containing supercooled water droplets, ice accretion can occur on the windward side of the aircraft, including the nose, wings, engine inlets and other critical locations[1]. Aircraft icing is a significant hidden hazard that can lead to aviation accidents. If icing occurs on the leading edge of the wing, it can cause the streamlined shape to become non-streamlined, resulting in vortex separation of the airflow, significantly reducing lift and increasing drag[2]. Flight parameters of the aircraft and clouds parameters in the airflow are the key influencing factors in aircraft icing. Numerical simulation technology is one of the effective means to obtain the spatial distribution of icing cloud parameters, such as liquid water content (LWC), median volumetric diameter(MVD)[3-4].

Using traditional high-fidelity numerical simulation to calculate icing cloud parameters is often very time-consuming, which limits the practical application of this method. Computational methods based on surrogate/reduced-order models have been widely applied in engineering practice due to their ability to effectively handle numerical solutions of high-precision complex systems[5-6]. Such models are obtained by approximating multi-dimensional nonlinear time-varying physical processes with low-dimensional descriptions and expressing the characteristics of the original physical problems with fewer degrees of freedom, thereby achieving the goal of simplifying the model and improving computational efficiency. Proper orthogonal decomposition (POD) is a

*Corresponding author, E-mail address: yixian@cardc.cn.

How to cite this article: LI Tingyu, REN Jinghao, WANG Qiang, et al. Fast calculation of icing cloud parameters based on POD_Kriging surrogate model[J]. Transactions of Nanjing University of Aeronautics and Astronautics, 2023, 40(S1): 1-12.
http://dx.doi.org/10.16356/j.1005-1120.2023.S1.001

representative class of model reduction method in Refs.[7-8].

POD reduced-order models can be classified into two types: intrusive and non-intrusive model reduction. Intrusive model reduction involves expressing the key physical fields in terms of a series of optimal orthogonal bases and corresponding coefficients. The original governing equations are then projected onto the low-dimensional space to establish the reduced-order model (ROM)[9-10]. A lot of mathematical derivation and equation discretization are requires in this modeling strategy, so it is difficult to implement.

Non-intrusive model reduction does not rely on the original governing equations, but instead establishes a surrogate model between the input and output of the dynamical system[11-12]. By utilizing the surrogate model, the POD orthogonal basis coefficients corresponding to different parameters can be rapidly computed. The computation of common orthogonal basis coefficients can be mainly divided into two categories. One is the interpolation method, which approximates the evolution of the orthogonal basis coefficients by constructing a spatiotemporal hypersurface interpolation function. Common methods include radial basis function (RBF)[13], Kriging[14], multivariate interpolation[15] and Gaussian process[16]. The other is the neural network model[17-18]. By utilizing the powerful nonlinear mapping ability and highly self-learning ability of neural networks, the mapping relationship between input parameters and orthogonal basis coefficients can be established. Since non-intrusive model reduction relies only on sample data and does not consider the actual physical process, its computational accuracy and generalization ability are lower than that of intrusive model reduction. With the rapid development of artificial intelligence and big data technology, in order to improve the practicality of non-intrusive surrogate models under neural network frameworks, different degrees of physical knowledge constraints have been introduced in the network training process[19-20].

At present, non-intrusive order reduction method has been applied to aircraft icing prediction[6-7,18]. By constructing the mapping relationship between flight parameters, cloud parameters and ice shape coordinate points, quasi-steady ice shape prediction under different input parameters can be realized. This method ignores the whole physical process of icing, and its accuracy needs to be further improved. Another alternative method is to quickly calculate the cloud parameters (such as droplet collection coefficient) required for ice accretion by surrogate model, while the growth of ice shape still adopts high-fidelity numerical simulation method. Therefore, this paper proposes to use POD and Kriging surrogate method to establish a fast prediction model for icing cloud parameters, which can improve the calculation efficiency of traditional icing numerical simulation methods while ensuring the accuracy of icing calculation.

The paper is organized in three parts: the computaional methods are proposed in the first section, including sampling method, theoretical knowledge of POD and Kriging model and solution process. Section 2 is the central part of the paper, where the detailed assessment and discussion of the proposed POD_Kriging model are presented by using the NACA0012 airfoil. Compared with the commercial software FENSAP-ICE, the calculation efficiency and accuracy of the proposed surrogate model are verified. The concluding remarks and future work are given in the final part.

1 Computational Methods

1.1 Sample calculation based on FENSAP-ICE and NNW-ICE

The calculation and prediction accuracy of the surrogate model is highly dependent on the selected sample data. In order to calculate the flow fields and the water droplet impingement around the airfoil, the FENSAP and DROP3D modules from the commercial software FENSAP-ICE were first used. For the air flow simulation, the Spalart-Allmaras model was employed for the Reynolds average Navier-Stokes (RANS) turbulence equations. The Eulerian two-fluid model is used for the water droplet impingment calculations, which consists of Euler and droplet-related continuity and momentum equations[3]

$$\frac{\partial \alpha}{\partial t}+\nabla\cdot(\alpha \boldsymbol{u}_{\mathrm{d}})=0 \tag{1}$$

$$\frac{\partial \boldsymbol{u}_{\mathrm{d}}}{\partial t}+\boldsymbol{u}_{\mathrm{d}}\nabla\cdot\boldsymbol{u}_{\mathrm{d}}=\frac{C_{\mathrm{D}}Re_{\mathrm{d}}}{24K}(\boldsymbol{u}_{\mathrm{a}}-\boldsymbol{u}_{\mathrm{d}})+\left(1-\frac{\rho_{\mathrm{a}}}{\rho_{\mathrm{w}}}\right)\frac{1}{Fr^{2}}g \tag{2}$$

where α is the non-dimensional water volume fraction; $\boldsymbol{u}_{\mathrm{d}}$ the droplet velocity; $\boldsymbol{u}_{\mathrm{a}}$ the air velocity; t the time; ρ_{a} the air density; ρ_{w} the water density; Re_{d} the dimensionless water droplet Reynolds number, and ρ the density. The first and second right-hand-side term of Eq.(2) is the air drag force on the droplets and the buoyancy and gracity forces. The inertial parameter K and the Fround number are defined as

$$K=\rho_{\mathrm{w}}d_{\mathrm{w}}^{2}\boldsymbol{u}_{\mathrm{a},\infty}/(18L\mu_{\mathrm{a}}) \tag{3}$$

$$Fr=\boldsymbol{u}_{\mathrm{a},\infty}/\sqrt{Lg} \tag{4}$$

where d_{w} is the droplet diameter; $\boldsymbol{u}_{\mathrm{a},\infty}$the far-field velocity; L the characteristice length; μ_{a} the dynamic viscosity of air; and g the acceleration of gravity.

In Eq.(2), C_{D} is the drag coefficient for the spherical droplets

$$C_{\mathrm{D}}=\begin{cases}\dfrac{24(1+0.15Re_{\mathrm{D}}^{0.687})}{Re_{\mathrm{D}}} & Re_{\mathrm{D}}\leqslant 1\,300\\ 0.4 & \text{Otherwise}\end{cases} \tag{5}$$

where $Re_{\mathrm{D}}=\rho_{\mathrm{w}}d_{\mathrm{w}}\boldsymbol{u}_{\mathrm{a},\infty}|\boldsymbol{u}_{\mathrm{d}}-\boldsymbol{u}_{\mathrm{a}}|/\mu_{\mathrm{a}}$.

Based on the resolved α and $\boldsymbol{u}_{\mathrm{d}}$ through the whole solution domain, the local collection efficiency β can then be obtained on the surface, shown as

$$\beta=-\alpha\boldsymbol{u}_{\mathrm{d}}\cdot\boldsymbol{n} \tag{6}$$

where $\boldsymbol{n}$ is the normal vector on solid surface.

According to the spatial distribution of the LWC and the collection efficiency β obtained by the FENSAP-ICE, the NNW-ICE software developed by the China Aerodynamics Research and Development Center(CARDC) was employed to extract the distribution of LWC and β on the surface as the sample data.

1.2 POD method

POD is a data processing method with high computational speed and accuracy. It can provide a set of optimal orthogonal basis in the sense of least squares to linearly approximate the physical field for the specific physical problem. The physical field (such as LWC, β) obtained by the above numerical simulation can be expressed as follows

$$f(\boldsymbol{x})=\sum_{k=1}^{M}a_{k}\phi_{k}(\boldsymbol{x}) \tag{7}$$

where α_k is the kth spectral coefficient; $\phi_k(x)$ the kth basis functions or POD modes, which is only space-dependent; $f(\boldsymbol{x})$ the original physical field, i.e. sample data; and M the number of basis functions.

The POD "Snapshot" method proposed by Sirovich[8] was used to obtain the basis functions. According to the selected sample data, the correlation matrix $\boldsymbol{R}$ is defined as

$$\boldsymbol{R}=\boldsymbol{C}_{\mathrm{s}}^{\mathrm{T}}\boldsymbol{C}_{\mathrm{s}} \tag{8}$$

where $\boldsymbol{C}_s=[f_1(\boldsymbol{x})\quad f_2(\boldsymbol{x})\quad\cdots\quad f_N(\boldsymbol{x})]$ is the sample matrix.

The eigenvalue λ and eigenvector $\boldsymbol{V}$ can be obtained by eigenvalue decomposition of correlation matrix $\boldsymbol{R}$, shown as

$$\boldsymbol{R}\boldsymbol{V}=\begin{bmatrix}\lambda_1 & & & \\ & \lambda_2 & & \\ & & \ddots & \\ & & & \lambda_N\end{bmatrix}\boldsymbol{V} \tag{9}$$

The POD modes can be calculated by using the eigenvector $\boldsymbol{V}$ and the sample matrix $\boldsymbol{C}_{\mathrm{s}}$, shown as

$$\boldsymbol{\Psi}=\boldsymbol{C}_{\mathrm{s}}\boldsymbol{V}/\|\boldsymbol{C}_{\mathrm{s}}\boldsymbol{V}\| \tag{10}$$

where $\boldsymbol{\Psi}=[\phi_1\quad\phi_2\quad\cdots\quad\phi_N]$, and $\|\cdot\|$ represents the L^2 norm.

As shown in Eq.(11), the spectral coefficients can be given by multiplying the POD modes onto the original sample.

$$\boldsymbol{\alpha}_k=(\boldsymbol{f}(\boldsymbol{x}),\phi_k(\boldsymbol{x})) \tag{11}$$

The selected POD mode is generally judged by the eigenvalue λ_i, which can be seen as an indicator of the energy contained in this mode. The energy contribution of the ith basis function is defined as

$$\xi_i=\lambda_i\Big/\sum_{j=1}^{N}\lambda_j \tag{12}$$

The cumulative energy contribution of the first M POD modes is

$$\eta_k=\sum_{k=1}^{M}\lambda_k\Big/\sum_{j=1}^{N}\lambda_j \tag{13}$$

The different ξ_i in Eq.(12) can be used to sort the corresponding POD modes, and η_k in Eq.(13)

helps us to determine the number of POD modes for data prediction of the surrogate model. Actually, whether the number of POD modes selected is too larger or too small will affect the calculation accuracy of the surrogate model. Too few POD modes will cause the loss of characteristic scale and key information of physical problems, while too many POD modes will introduce data errors. The truncation criterion of the POD modes generally satisfies $\eta_k \geqslant 99\%$.

1.3 Kriging method

Kriging interpolation algorithm is also called local estimation interpolation or spatial local interpolation. Suppose that the attribute value of a certain research variable $\{Z(\boldsymbol{x})\}$ at a space point $x_i \in \Omega$ is $Z(x_i)$, then the Kriging estimate of the attribute value $Z(x_0)$ of the point $x_0 \in \Omega$ is linear weighted sum of the known sampling points in the finite space region[21], shown as

$$\hat{Z}(x_0) = \sum_i^M w_i Z(x_i) \tag{14}$$

As can be seen from the above formula, the key of Kriging interpolation algorithm is to find the weight coefficient w_i. According to the ordinary Kriging interpolation principle, the weight w_i must satisfy the unbiased estimation condition to minimize the estimation variance

$$\begin{cases} E\left[\hat{Z}(x_0) - Z(x_0)\right] = 0 & \text{Unbiasedness} \\ \mathrm{Var}\left[\hat{Z}(x_0) - Z(x_0)\right] \to \min & \text{Minimum-variance} \end{cases} \tag{15}$$

The above equation is an extremum problem under certain conditions, which can be solved by the standard Lagrangian multiplier method

$$\begin{cases} \sum_{j=1}^M w_j C(x_i, x_j) - \mu = C(x_i, x_0) \\ \sum_{i=1}^M w_i = 1 \end{cases} \tag{16}$$

where $C(x_i, x_j) = \mathrm{Cov}(x_i, x_j)$ is the covariance function, and μ the Lagrange multiplier. The relationship between the covariance function and the semi-variance function $\gamma(h)$ is as follows

$$\gamma(h) = C(0) - C(h) \tag{17}$$

where $C(0)$ is the variance of the regionalized variable $Z(x)$, and h the relative distance.

According to Eq.(17), Eq.(16) can also be expressed as a function of $\gamma(h)$

$$\begin{cases} \sum_{j=1}^M w_j \gamma(x_i, x_j) + \mu = \gamma(x_i, x_0) \\ \sum_{i=1}^M w_i = 1 \end{cases} \tag{18}$$

The above equation can be written in matrix form as

$$\begin{bmatrix} \boldsymbol{C} & \boldsymbol{D} \\ \boldsymbol{D}^{\mathrm{T}} & 0 \end{bmatrix} \begin{bmatrix} w \\ \mu \end{bmatrix} = \begin{bmatrix} \boldsymbol{b} \\ 1 \end{bmatrix} \tag{19}$$

where w is the weight coefficient; $\boldsymbol{D} = [1 \quad 1 \quad \cdots \quad 1]^{\mathrm{T}}$; $\boldsymbol{C} = \begin{bmatrix} C(x_1, x_1) & \cdots & C(x_1, x_M) \\ \vdots & & \vdots \\ C(x_M, x_1) & \cdots & C(x_M, x_M) \end{bmatrix}$; $\boldsymbol{b} = \begin{bmatrix} C(x_1, x_0) \\ \vdots \\ C(x_n, x_0) \end{bmatrix}^{\mathrm{T}}$.

The distribution of weight coefficient w_i can be obtained by solving the above matrix equation, and then the point to be interpolated can be obtained by substituting it into Eq.(19). The test variation function is the function of the relative distance between space points x_i and x_j, which can be calculated by the Euclidean distance, that is

$$\gamma(x_i, x_j) = \gamma^P(|x_i - x_j|) = \gamma^P(h_s) \tag{20}$$

where γ_p is the theoretical variation function; $|\cdot|$ the Euclidean distance; and h_s the space distance.

In fact, the theoretical variation function can be fitted by the experimental variation function and the spatial point pairs (Table 1), where C_0 is the nugget value, B, a and b are the constants, and C is the partial still. For the linear model, if $B=0$, it means a pure nugget effect. Commonly used theoretical models can be divided into linear model, spherical model, exponential model, Gaussian model.

1.4 Surrogate model of POD_Kriging

The overall construction process of surrogate model of POD_Kriging is shown in Fig.1. The input of the model is a series of cloud and flight parameters (Outside air temperature (OTA), altitude (ALT), air speed, angle of attack (AoA), median volumetric diameter (MVD) of droplets and LWC), and the output is approximate cloud field (LWC and β). The main modeling processes are:

Table 1 Theoretical model of spatial variograms

Theoretical model	Function expression
Linear model	$\gamma(h_s)=\begin{cases} C_0 & h_s=0 \\ Bh_s & 0<h_s<a \\ C_0+C & h_s\geqslant a \end{cases}$
Spherical model	$\gamma(h_s)=\begin{cases} C_0 & h_s=0 \\ C_0+C\left[3h_s/2a-0.5\left(h_s/a\right)^3\right] & 0<h_s<a \\ C_0+C & h_s\geqslant a \end{cases}$
Exponential model	$\gamma(h_s)=\begin{cases} 0 & h_s=0 \\ C_0+C\left[1-\exp(-h_s/a)\right] & h_s\neq 0 \end{cases}$
Gaussian model	$\gamma(h_s)=\begin{cases} 0 & h_s=0 \\ C_0+C\left[1-\exp(-9h_s^2/a^2)\right] & h_s\neq 0 \end{cases}$

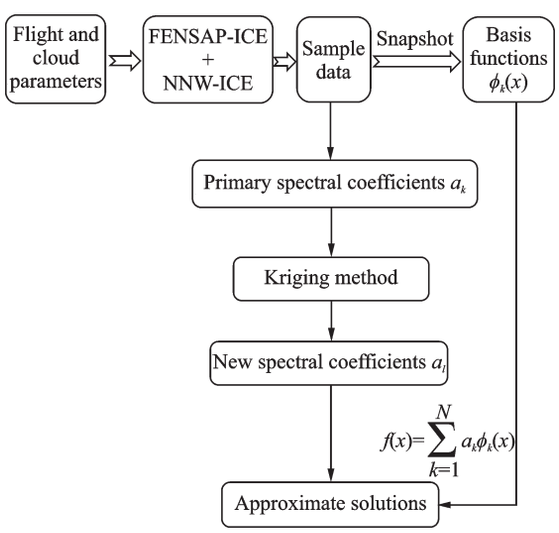

Fig.1 Surrogate model of POD_Kriging

(1) According to the input flight and cloud parameters, the sample set is first resolved by the FENSAP-ICE and NNW-ICE.

(2) Calculate the POD basis functions $\phi_k(x)$ via POD "snapshot" method based on the selected sample set.

(3) The primary spectral coefficient a_k corresponding to the basis function $\phi_k(x)$ is obtained through Eq.(11).

(4) By changing the input conditions, the new spectral coefficients a_l can be interpolated by the Kriging method.

(5) According the interpolated spectral coefficients a_l and the corresponding to POD modes, the approximate or predicted physical field is reconstructed by Eq.(7).

2 Assessment and Discussion of the POD_Kriging Surrogate Method

To evaluate the accuracy of reconstruction and prediction for the proposed POD_Kriging surrogate model, a quasi-three-dimensional NACA0012 airfoil model is adopted. The computational mesh, as displayed in Fig.2, consists of 242 788 hexahedral cells and 487 600 nodes. The airfoil surface contains 406 quadrilateral wall faces and 814 nodes.

To enrich the sampling space, six design variables have been selected: OTA, ALT, air speed,

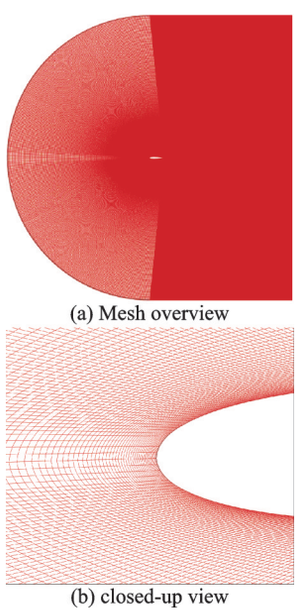

Fig.2 Computational mesh of NACA0012

AoA, MVD and LWC. The range of parameter changes is shown in Table 2. The total number of samples is 486. Base on this case, we will use the following three physical fields to verify the prediction accuracy of the POD_Kriging method. The first is the LWC distribution in the whole computational domain, and the rest is the LWC and β distribution on the airfoil surface.

Table 2 Six expreimental parameters with their corresponding ranges

Parameter	OAT/℃	Altitude/m	Air speed/(m•s^{-1})	AOA/(°)	MVD/μm	LWC/(g•m^{-3})
Minmum	−5	2 000	90	0	20	0.5
Maximum	−20	4 000	130	4	60	1.5

In order to quantitatively verify the accuracy of the surrogate model, the following two error criteria are defined.

The root mean squared error (RSME) is

$$\mathrm{RSME}=\sqrt{\frac{1}{N_s}\sum_{i=1}^{N_s}\left|\hat{f}(x_i)-f(x_i)\right|^2} \tag{21}$$

The mean absolute error (MAE) is

$$\mathrm{MAE}=\frac{1}{N_s}\sum_{i=1}^{N_s}\left|\hat{f}(x_i)-f(x_i)\right| \tag{22}$$

where N_s is the total number of sample; $\hat{f}(x_i)$ and $f(x_i)$ represent the results of the POD_Kriging and FENSAP-ICE, respectively. ASME is sensitive to too large or too small errors, reflecting the precision of model prediction. MAE reflects the magnitude of prediction error of surrogate model.

As shown in Table 3, five test cases with their corresponding parameter values are selected to evaluate the performance of the surrogate model. Case 1 is used to test the influence of the spatial variograms on the calculation results of the surrogate model. Case 2 and Case 3 are used to test the reconstruction accuracy of the POD_Kriging model. Case 4 and Case 5 are used to verify the prediction accuracy of the surrogate model.

Table 3 Five test cases with their corresponding parameter values

Case	OAT/℃	Altitude/m	Air speed/(m•s^{-1})	AOA/(°)	MVD/μm	LWC/(g•m^{-3})
1	−20	2 000	110	0	20	0.5
2	−10	2 000	130	2	40	1.0
3	−5	4 000	90	4	60	1.5
4	−7	2 500	120	3.5	50	0.8
5	−15	3 000	125	2.5	45	1.2

2.1 LWC predicion

Since the spatial variograms is critical to the prediction accuracy of the POD_Kriging surrogate model, we first verified the impact of the three kind of popular theoretical model in Table 3 on the calculation results. As we can see from Fig.3, the LWC and β on the surface calculated by using the three theoretical model are basically consistent. Therefore, the spherical model is selected as the spatial variogram in the test.

For the LWC prediction of the whole computational domain, the energy contribution and cumulative energy contribution of POD mode are displayed in Fig.4. The energy proportion of the first POD mode is 96.32%, which is higher than the remaining modes. The cumulative energy contribution of the first six POD modes is 99.79%. The total energy contribution of the first twenty POD modes is 99.99%. Base on Case 2, the MAE and RMSE convergence with increasing number of POD mode are presented in Fig.5. It can be seen that when the number of POD modes is greater than 10, the two groups of errors calculated by the POD_Kriging surrogate model tend to be stable. Therefore, according to the basis function truncation criterion, the first twenty modes are employed for reconstruction of full field LWC.

Fig.6 shows the comparisons of reconstructed LWC between FENSAP-ICE and POD_Kriging surrogate model. It can be seen from Figs.6(a, b),

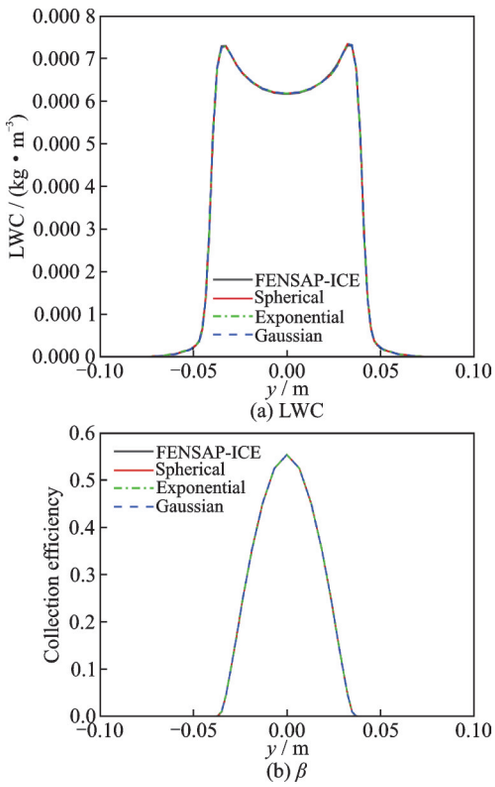

Fig.3 Sensitivity of different spatial variograms to the reconstruction effect of POD_Kriging model

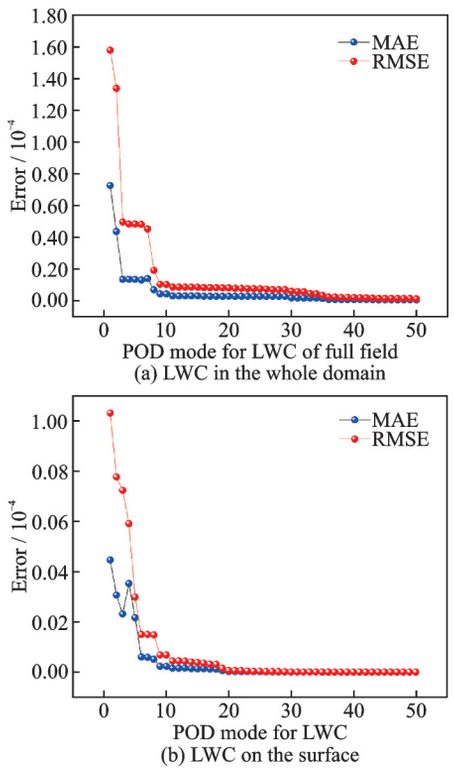

Fig.5 Mean absolute error and root mean squared error convergence with increasing number of POD mode

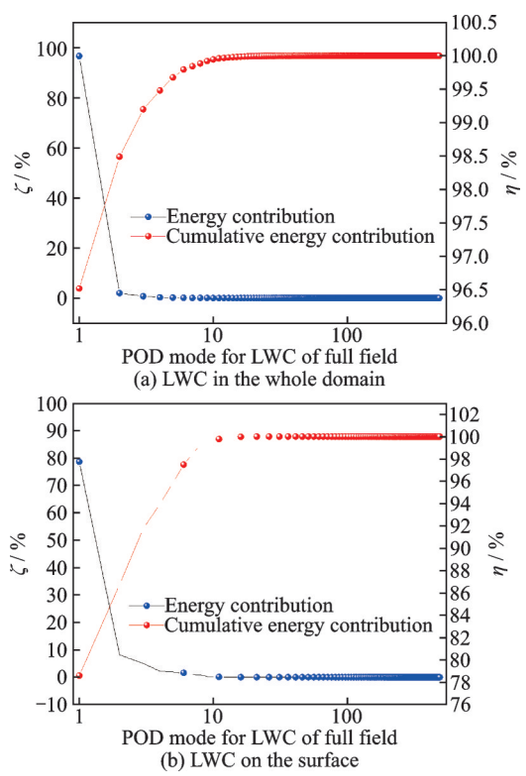

Fig.4 Energy contribution and cumulative energy contribution with increasing number of POD mode

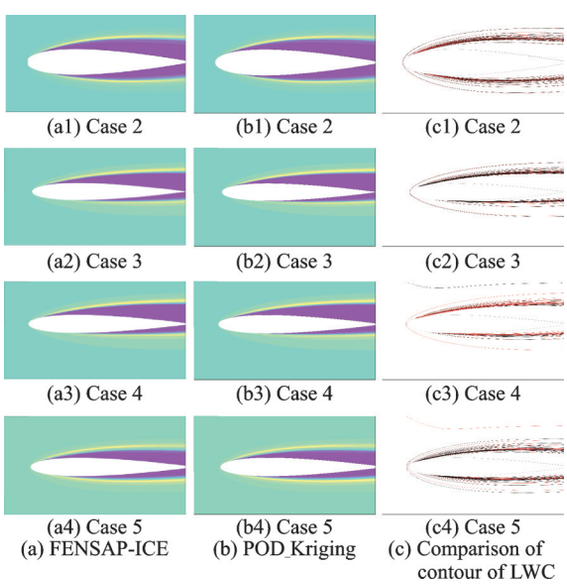

Fig.6 Comparisons of reconstructed LWC between FENSAP-ICE and POD_Kriging

the LWC spatial distribution of the two sets of results in the four cases is basically the same. It can be clearly seen from Fig.6(c) that the calculation difference between the two groups of results. In Fig.6(c), the black solid line represents the result of FENSAP-ICE; the red dashed line represents the result of POD_Kriging. The MAE and RMSE of reconstruction and prediction results are shown in Table 4. The maximum values of MAE and RMSE for surrogate model are the 0.046% and 0.069%, respectively.

Table 4 Construction and prediction error for full field LWC

Case	2	3	4	5
MAE/%	1.32×10^{-4}	2.67×10^{-4}	0.046	0.015
RSME/%	4.13×10^{-4}	7.95×10^{-4}	0.069	0.021

For the LWC prediction on the surface, it can be seen from Fig.4(b) that the energy contribution of the first POD mode is 78.60%. The first three POD modes have a total energy of over 90%. The cumulative energy contribution of the first 17 modes is close to 100%. Fig.5(b) shows the convergence process of MAE and RSME with the number of POD modes. When the number of POD modes is greater than 20, MAE and RSME tend to be consistent. Thus, we still select the first 20 POD modes for surface LWC prediction. As can be seen from Fig.7, the accuracy of surrogate model reconstruction is higher than that of prediction. The construction and prediction errors for surface LWC are shown in Table 5. In the four cases, the maximum value of model prediction error is MAE=4.46×10^{-3}% and RSME 1.03×10^{-2}%.

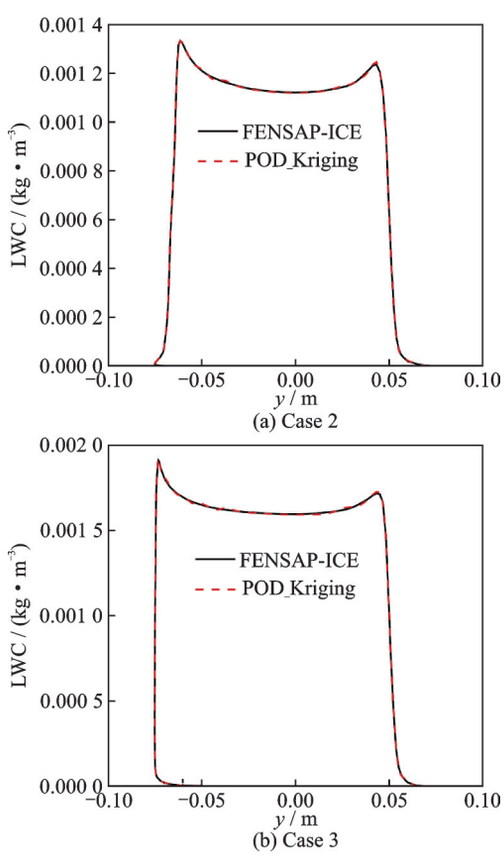

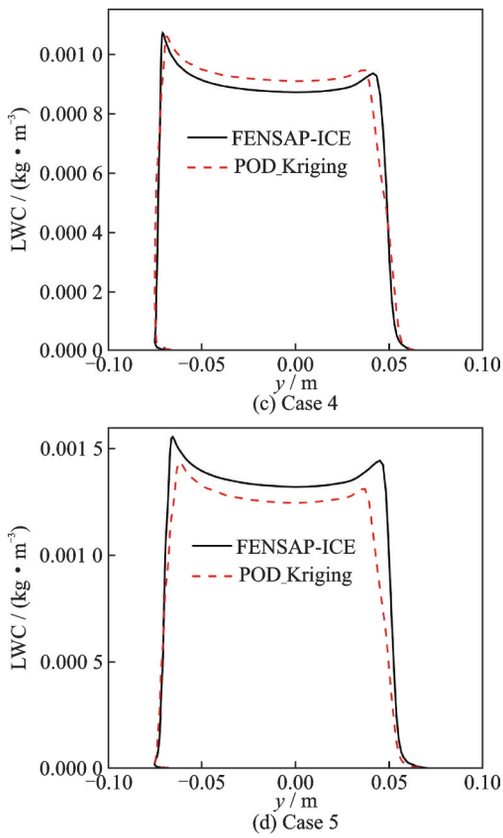

Fig.7 Comparisons of reconstructed LWC at the surface between FENSAP-ICE and POD_Kriging

Table 5 Construction and prediction error for surface LWC

Case	2	3	4	5
MAE/%	6.51×10^{-5}	1.53×10^{-4}	4.46×10^{-3}	3.89×10^{-3}
RSME/%	1.73×10^{-4}	3.24×10^{-4}	1.03×10^{-2}	1.10×10^{-2}

2.2 Droplet collection efficiency predicion

The proposed POD_Kriging surrogate model is used to predict the collection efficiency (β) in this Section. Fig.8 shows the variation of the energy captured by the basis functions against the number of POD modes. The first POD mode contains 95.12% of the total energy. Most energy over 99% is captured within the first ten modes. When the cumulative energy contribution approaches 100%, 15 POD modes are required. Under the condtion of Case 2, Fig.8 displays the variation of the reconstructed error varying with the number of POD modes. When the number of POD modes is less than four, the error will oscillate and then decrease rapidly with the increase of the number of POD modes. In order to

balance accuracy and computaional efficiency, 15 POD modes are selected for collection coefficiency prediction.

Fig.9 shows the comparisons of reconstructed and predicted collection efficiency at the surface between FENSAP-ICE and POD_Kriging. The results suggest that there is almost no difference between the original and reconstructed solutions using only 15 of the available POD modes. It indicates that the 15 POD modes is sufficient to obtain the droplet impingement limit and slope of the collection efficiency. The errors of construction and prediction results are shown in Table 6. For MAE, the maximum reconstruction and prediction errors are $3.90\times10^{-3}\%$ and 0.25%, respectively. For RSME, the maximum reconstruction and prediction errors are $1.15\times10^{-2}\%$ and 0.82%, respectively. Both errors can meet the actual needs, reflecting the good adaptability of the surrogate model.

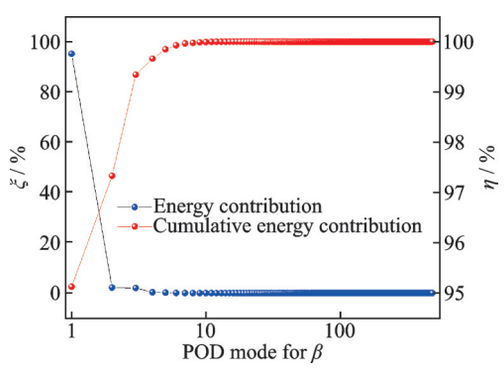

Fig.8 Energy contribution and cumulative energy contribution with increasing number of POD modes

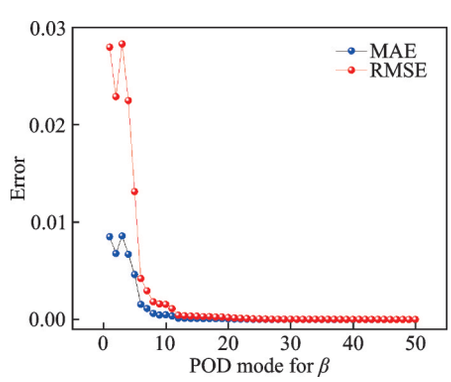

Fig.9 MAE and RMSE convergence with increasing number of POD modes

Table 6 Error of construction and prediction results of surface β

Case	2	3	4	5
MAE/%	3.61×10^{-3}	3.90×10^{-3}	0.25	0.24
RSME/%	1.15×10^{-2}	1.12×10^{-2}	0.64	0.82

2.3 Computational efficiency discussion

A good surrogate model not noly needs high calculation accuracy, but also needs fast calculation speed. For the FENSAP-ICE, the computational cost mainly contains two parts: Outflow field solution and droplet impingement solution. A workstation with an Intel Xeon Gold 6248R CPU, 3.0 GHz, processor with a 35.75 MB L3 cache is used to solve the system of equations. The CPU time taken by all-time steps is 1 487.8 s. In the POD_Kriging approach, the computational cost mainly include the calculation of POD modes and spectral coefficient interpolation. Once the snapshots data are complete, the calculation of the POD modes can be viewed as an off-line operation.

The comparison of computational speed for LWC and β between FENSAP-ICE and POD_Kriging is shown in Table 7 and Table 8. It can be seen that, with the increase of the number of POD modes, the surrogate model will not increase much computation cost. Compared with the FENSAP-ICE, the average speed-up ratio of the surrogate model for the calculation of surface LWC and β can reach 115 times. For full field LWC calculation, the surrogate model can still improve the calculation efficiency by 39 times on average.

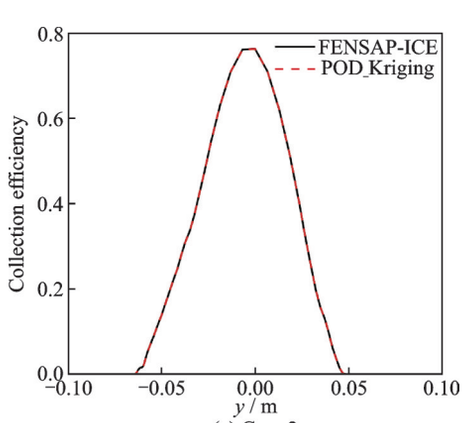

(a) Case 2

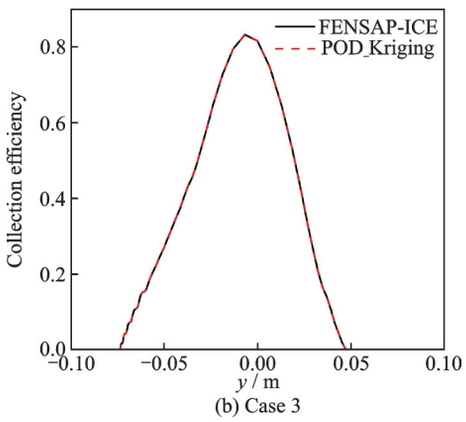

(b) Case 3

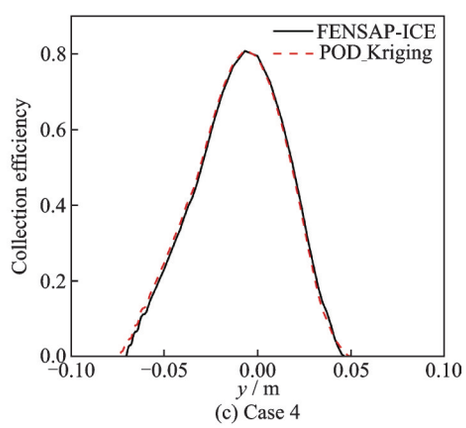

(c) Case 4

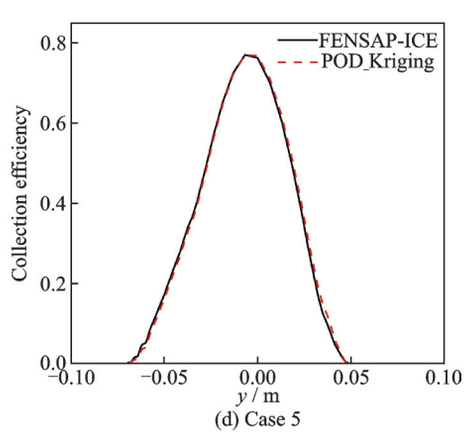

(d) Case 5

Fig.10 Comparisons of reconstructed collection efficiency at the surface between FENSAP-ICE and POD_Kriging

Table 7 Comparison of computational speed for LWC and β at surface between FENSAP-ICE and POD_Kriging

Case	Time cost / s				Speed-up ratio
	FENSAP-ICE	POD_Kriging			
		ϕ_1^1	ϕ_1^{15}	ϕ_1^{20}	
2	1 484.2	11.6	12.7	13.1	114.3
3	1 488.7	11.8	12.8	12.9	115.3
4	1 492.5	11.5	12.6	12.8	116.4
5	1 485.6	11.5	12.5	12.9	115.6
Average	1 487.8	11.6	12.0	12.9	115.4

Table 8 Comparison of computational speed for full field LWC between FENSAP-ICE and POD_Kriging

Case	Time cost / s				Speed-up ratio
	FENSAP-ICE	POD_Kriging			
		ϕ_1^1	ϕ_1^{15}	ϕ_1^{20}	
2	1 484.2	22.9	33.8	38.3	38.7
3	1 488.7	22.3	35.1	37.3	39.9
4	1 492.5	22.8	33.2	37.2	40.1
5	1 485.6	23.5	33.8	38.4	38.7
Average	1 487.8	22.9	34.0	37.8	39.3

3 Conclusions

The present work proposes a surrogate model for fast calculation of icing cloud parameters by using POD and Kriging methods. Precision and acceleration of the POD_Kriging model are discussed under different flight and cloud parameter conditons. The primary conclusions and remarks are as follows:

(1) The speed-up ratio is very large with very high predicition precision for caculation of liquid water content and droplet collection efficiency in different types of input parameters. The mean absolute error and root mean squared error are within the acceptable range (MAE=6.51 × 10^{-5}%—0.25%, RSME=1.73×10^{-4}%—0.82%). Compared to FENSAP-ICE, the computational efficiency of POD_Kriging model can be improved at least 39 times on average.

(2) The number of POD modes and spatial variogram have little effect on the computational efficiency of the POD_Kriging model. The energy proportion of the first POD mode is often dominant, but can contain only limited information. The selection of POD modes should be measured according to the error convergence proecss and computational efficiency.

(3) Although the 2-D test example is used in this paper, the proposed POD_Kriging surrogate model has the potential to realize the fast calculation of three-dimensional icing cloud fields in complex regions.

References

[1] LYNCH F T, KHODADOUST A. Effects of ice accretions on aircraft aerodynamics[J]. Progress in Aerospace Science, 2001, 37(8): 669-767.

[2] THOMAS S K, CASSONI R P, MACARTHUR C D. Aircraft anti-icing and de-icing techniques and modeling[J]. Journal of Aircraft, 2012, 33(5): 841-854.

[3] BEAUGENDRE H, MORENCY F, HABASHI W G. FENSAP-ICE's three-dimensional in-flight ice accretion module: ICE3D[J]. Journal of Aircraft, 2003, 40(2): 239-247.

[4] CAO Y, ZHANG Q, SHERIDAN J. Numerical simulation of rime ice accretions on an aerofoil using an Eulerian method[J]. The Aeronautical Journal, 2008, 112(1131): 243-249.

[5] SHEN X B, ZHAO W Z, QI Z C, et al. Analysis of numerical methods for droplet impingement characteristics under aircraft icing conditions[J]. Aerospace, 2022, 9: 416.

[6] JUNG S K, SHIN S, CHO T H. An efficient CFD-based method for aircraft icing simulation using a reduced order model[J]. Journal of Mechanical Science and Technology, 2011, 25(3): 703-711.

[7] FOSSATI M, HABASHI W G. Multiparameter analysis of aero-icing problems using proper orthogonal decomposition and multidimensional interpolation[J]. AIAA Journal, 2013, 51(4): 946-960.

[8] SIROVICH L. Turbulence and the dynamics of coherent structure. Part I: Coherent structures[J]. Quarterly of Applied Mathematics, 1987,45: 561-571.

[9] AKKARI N, MERCIER R, LARTIGUE G, et al. Stable POD-Galerkin reduced order models for unsteady turbulent incompressible flows[C]//Proceedings of the 55th AIAA Aerospace Sciences Meeting. [S.l.]:AIAA, 2017.

[10] PODVIN B. A proper-orthogonal-decomposition-based model for the wall layer of a turbulent channel flow[J]. Physics of Fluids, 2009, 21(1): 115.

[11] XIAO D, FANG F, BUCHAN A G, et al. Non-intrusive reduced order modelling of the Navier-Stokes equations[J]. Computer Methods in Applied Mechanics and Engineering, 2015, 293: 522-541.

[12] DUTTA S, FARTHING M W, PERRACCHIOHE E, et al. A greedy non-intrusive reduced order model for shallow water equations[J]. Journal of Computational Physics, 2021,439: 110378.

[13] DUDOUZE C, DE VUYST F, NAIR P B. Non-intrusive reduced-order modeling of parametrized time-dependent partial differential equations[J]. Numerical Methods for Partial Differential Equations, 2013, 29(5): 1587-1628.

[14] FOSSATI M. Evaluation of aerodynamic loads via reduced-order methodology[J]. AIAA Journal, 2015, 53(8): 2389-2405.

[15] WANG Y, BO Y, CAO Z, et al. A comparative study of POD interpolation and POD projection methods for fast and accurate prediction of heat transfer problems[J]. International Journal of Heat & Mass Transfer, 2012, 55(17/18): 4827-4836.

[16] YANG M, XIAO Z. POD-based surrogate modeling of transitional flows using an adaptive sampling in Gaussian process[J]. International Journal of Heat and Fluid Flow, 2020, 84: 108596.

[17] HESTHAVEN J S, UBBIALI S. Non-intrusive reduced order modeling of nonlinear problems using neural networks[J]. Journal of Computational Physics, 2018, 363: 55-78.

[18] STRIJHAK S, RYAZANOV D, KOSHELEV K, et al. Neural network prediction for ice shapes on airfoils using icefoam simulations[J]. Aerospace, 2022, 9: 96.

[19] CHEN W, WANG Q, HESTHAVEN J S, et al. Physics-informed machine learning for reduced-order modeling of nonlinear problems[J]. Journal of Computational Physics, 2021, 446: 110666.

[20] CHEN Y, HUANG D, ZHANG D, et al. Theory-guided hard constraint projection (HCP): A knowledge-based data-driven scientific machine learning method[J]. Journal of Computational Physics, 2021, 445: 110624.

[21] HAN Zhonghua. Kriging surrogate model and its application to design optimization: A review of recent progress[J]. Acta Aeronautica et Astronautica Sinica, 2016, 37(11): 3197-3225.(in Chinese)

Acknowledgements This work was supported in part by the National Natural Science Foundation of China (Nos. 12172372, 12132019) and the National Major Science and Technology Projects (No.J2019-III-0010-0054).

Authors Dr. **LI Tingyu** received his B.S.degree in oil-gas storage and transportation engineering from China University of Petroleum (Beijing) in 2017 and Ph.D. degree in power engineering and engineering Thermophysics from Xi'an Jiaotong University in 2021. His research interests include icing

numerical computaion, anti/de-icing technology and application of artificial intelligence in icing analysis, etc.

Prof. **YI Xian** received the B.S.degree from National University of Defense Technology and Ph. D. degree from China Aerodynamics Research and Development Center (CARDC). He is the director of Key Laboratory of Icing and Anti-icing of CARDC. His research interests include icing numerical computation, icing wind tunnel experimental technology and ice detection technology, etc.

Author contributions Dr. **LI Tingyu** interpreted the results and wrote the manuscript. Dr. **REN Jinghao** contributed to sample data based on NNW-ICE. Dr. **WANG Qiang** contributed to the discussion and background of the study. Prof. **YI Xian** designed the study and conducted the analysis. All authors commented on themanuscript draft and approved the submission.

Competing interests The authors declare no competing interests.

(Production Editor: SUN Jing)

基于POD_Kriging代理模型的结冰云雾参数快速计算方法研究

李庭宇[1,2], 任靖豪[1,2], 王 强[1,2], 易 贤[1,2]

(1.中国空气动力研究与发展中心低速空气动力研究所,绵阳 621000,中国;
2.中国空气动力研究与发展中心结冰与防除冰重点实验室,绵阳 621000,中国)

摘要:掌握结冰云雾参数的分布对于飞机结冰分析具有重要意义。为了获得这些参数,传统的高保真数值模拟技术计算效率低,难以应用于需要实时评估结冰的工程场景。为了克服这一困难,通过本征正交分解(Proper orthogonal decomposion, POD)方法与Kriging技术相结合,提出了一种非侵入式结冰云雾参数计算代理模型。该模型以4个飞行参数和2个云参数作为输入变量,模型输出为液体水含量(Liquid water content,LWC)和液滴收集系数。采用准三维NACA0012翼型验证了模型的准确性和计算效率。4个测试案例的数值结果表明:POD_Kriging模型准确、有效。相比于经典的FENSAP-ICE软件,所开发的代理模型能够更有效的得到结冰云雾场。

关键词:结冰云雾参数;代理模型;本征正交分解;Kriging;快速计算